# Nested self-similar wrinkling patterns in skins

KIRILL EFIMENKO[1], MINDAUGAS RACKAITIS[2]*, EVANGELOS MANIAS[2], ASHKAN VAZIRI[3], L. MAHADEVAN[3†] AND JAN GENZER[1†]

[1]Department of Chemical Engineering, North Carolina State University, Raleigh, North Carolina 27695-7905, USA
[2]Department of Materials Science & Engineering, Pennsylvania State University, University Park, Pennsylvania 16802, USA
[3]Division of Engineering & Applied Sciences, Harvard University, Cambridge, Massachusetts 02138, USA
*Present address: Bridgestone/Firestone Research, Akron, Ohio 44317, USA
†e-mail: lm@deas.harvard.edu; Jan_Genzer@ncsu.edu

Published online: 6 March 2005; doi:10.1038/nmat1342

**Stiff thin films on soft substrates are both ancient and commonplace in nature; for instance, animal skin comprises a stiff epidermis attached to a soft dermis. Although more recent and rare, artificial skins are increasingly used in a broad range of applications, including flexible electronics[1], tunable diffraction gratings[2,3], force spectroscopy in cells[4], modern metrology methods[5], and other devices[6–8]. Here we show that model elastomeric artificial skins wrinkle in a hierarchical pattern consisting of self-similar buckles extending over five orders of magnitude in length scale, ranging from a few nanometres to a few millimetres. We provide a mechanism for the formation of this hierarchical wrinkling pattern, and quantify our experimental findings with both computations and a simple scaling theory. This allows us to harness the substrates for applications. In particular, we show how to use the multigeneration-wrinkled substrate for separating particles based on their size, while simultaneously forming linear chains of monodisperse particles.**

Wrinkling, buckling and other mechanical instabilities have been typically treated as a nuisance to be avoided rather than an exquisite pattern to be exploited. Although this view is changing with the growing understanding of how ubiquitous these phenomena are[9], the utilization of wrinkling in applications has been hampered by the absence of a detailed understanding of the phenomena, as well as the ability to control it experimentally. Here we focus on the tunable hierarchical wrinkling of model stiff elastomeric artificial skins supported on a soft base. These wrinkles are fabricated by uniaxially stretching poly(dimethyl siloxane) (PDMS) network sheets (thickness ~0.5 mm, Young modulus ~1 MPa)[10] in a custom-designed stretching apparatus[11] and exposing them to ultraviolet/ozone (UVO) radiation for extended periods of time (30–60 minutes). Previous studies established that the UVO treatment of PDMS converts the first ~5 nm of the PDMS surface into a stiff 'skin'[12], whose density is approximately a half of that of silica[13]. Optical microscopy and scanning force microscopy (SFM) experiments confirm that the surfaces are originally flat in the presence of strain.

After the UVO treatment, the strain is removed from the specimen and, the skin buckles perpendicularly to the direction of the strain. The buckle morphology depends on the strain removal rate. Specifically, stretched and UVO-modified specimens released at a fast rate (strain removed abruptly) contain a large number of structural defects (~1.17 defects per mm$^2$), typical for layered morphologies (see Fig. 1a). By decreasing the strain removal rate, the number of defects decreases dramatically. Simultaneously, cracks parallel to the strain direction appear on the sample surface. Figure 1b and c depicts optical microscopy images from samples whose strain removal rates were ~900 μm min$^{-1}$ (~0.47 defects per mm$^2$) and ~58 μm min$^{-1}$ (~0.15 defects per mm$^2$), respectively. Importantly, the buckle period stays the same within 5%, regardless of the strain removal rate. Work is currently underway that aims at understanding the mechanism of defect formation. Establishing

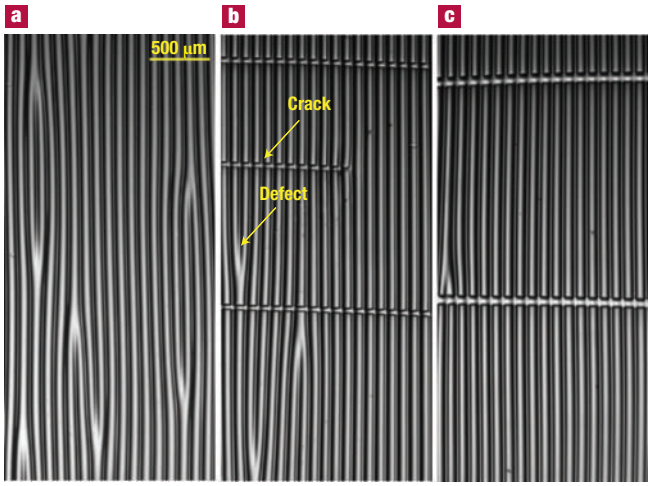


**Figure 1 Optical microscopy images taken in the transmission mode.** Samples prepared by stretching PDMS sheets by $\Delta = 50\%$, exposing them to UVO for 60 minutes and releasing the strain: **a**, instantaneously, and **b**,**c**, with the strain release rate of ~900 (**b**) and ~58 μm min$^{-1}$ (**c**). Note the different morphology of the substrates. The corresponding defect densities are: ~1.17 (**a**), ~0.47 (**b**), and ~0.15 defects per mm$^2$ (**c**). The approximate area of each defect is less than 0.1 mm$^2$.

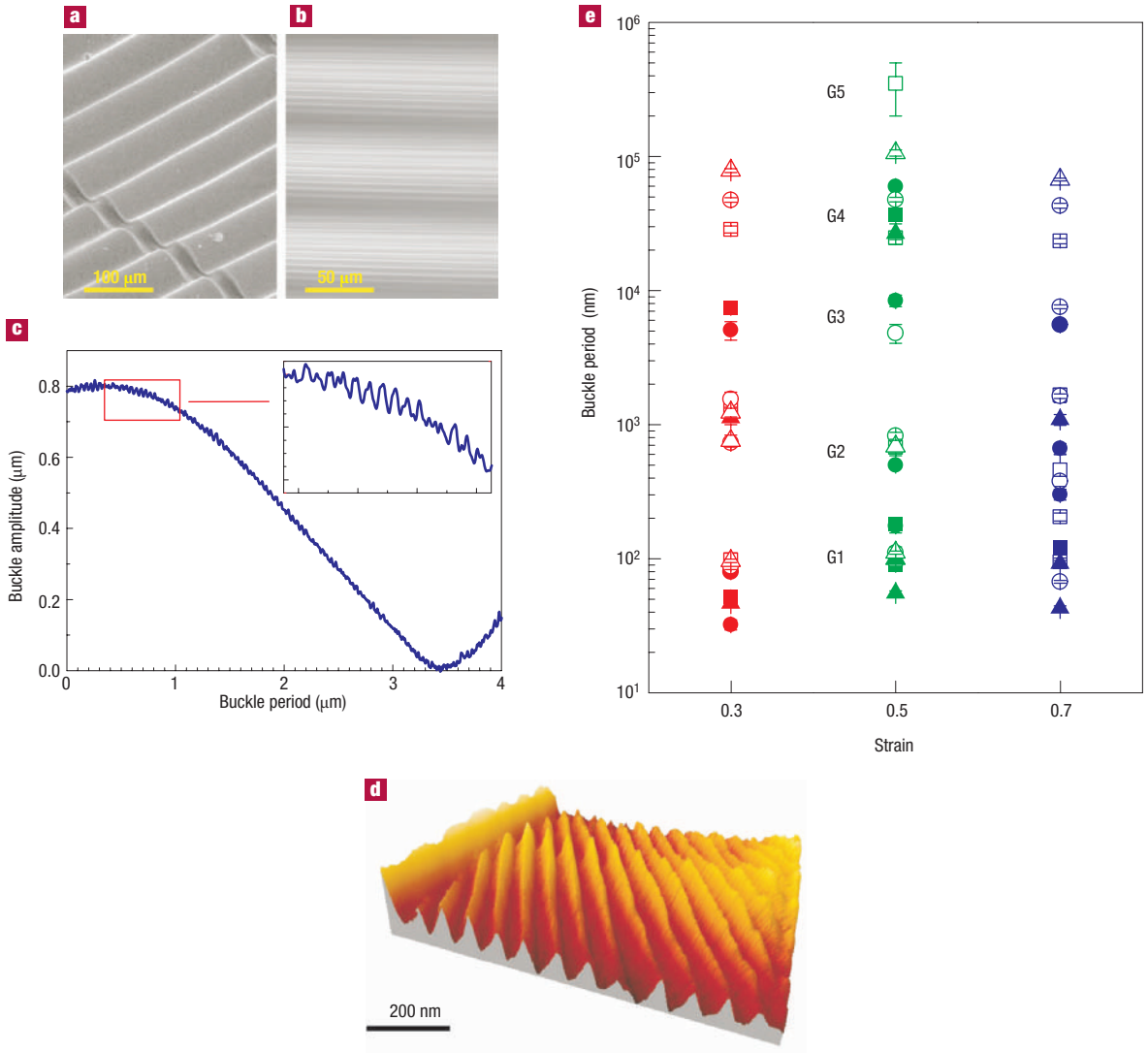


**Figure 2 Characterization of the nested hierarchy of buckles**. **a**, Scanning electron microscopy image of a buckle on PDMS substrate (covered with a ~4-nm-thick layer of platinum) revealing the G4 generation of buckles. **b**, Optical microscopy image in the transmission mode of G3 and G4 generations of buckles. **c**, Topography profile collected with profilometry on G2 (inset) and G3 (main figure) generations of buckles. **d**, Scanning force microscopy image revealing the structure of G1 buckles. **e**, Buckle period as a function of the strain imposed on the samples before the UVO treatment lasting for 30 (squares), 60 (circles), and 90 (up-triangles) minutes as measured by scanning force microscopy (filled symbols) and profilometry (open symbols). The error bars represent one standard deviation of the data.

the relationship between the defect density and the strain release rate would facilitate the generation of buckled substrates with minimal number of structural imperfections.

A detailed analysis of the buckled surface with SFM and profilometry uncover that the buckling patterns are hierarchical. Representative images depicting the various buckle generations are presented in Fig. 2. Buckles with smaller wavelengths (and amplitude) rest parallel to and within larger buckles, forming a nested structure. Figure 2e summarizes the SFM and profilometry results of the buckle periods. The data in Fig. 2e reveal that at least five distinct buckle generations (G) are present: the wavelengths of the generations ($\lambda$) are G1: ~50 nm, G2: ~1 μm, G3: ~5 μm, G4: ~50 μm, and G5: ~0.4 mm.

The mechanism of formation of the first generation of buckles, at the smallest scale, that is, ~50 nm, is as follows: The UVO treatment densifies the upper surface of the PDMS skin by proving additional crosslinks[12,13] and leads to an equilibrium (strain-free) configuration of the skin that resides on top of the flexible substrate, which is still under tensile strain. When this strain is relieved from the specimen, the substrate attempts to contract back to its strain-free configuration. However, the mismatch between the equilibrium strains of the stiff skin and the soft substrate prevents this from happening uniformly through the depth of the material. The competition between the bending-dominated deformations of the skin and the stretching/shearing-dominated deformations of the substrate cause the skin to wrinkle in response to the relaxation of the applied strain. Thus, the basic driving force behind wrinkling is the mismatch in the equilibrium states of the skin and the substrate. Although here this arises due to inhomogeneous crosslinking in the presence of strain, a similar phenomenon will take place in the presence of differential

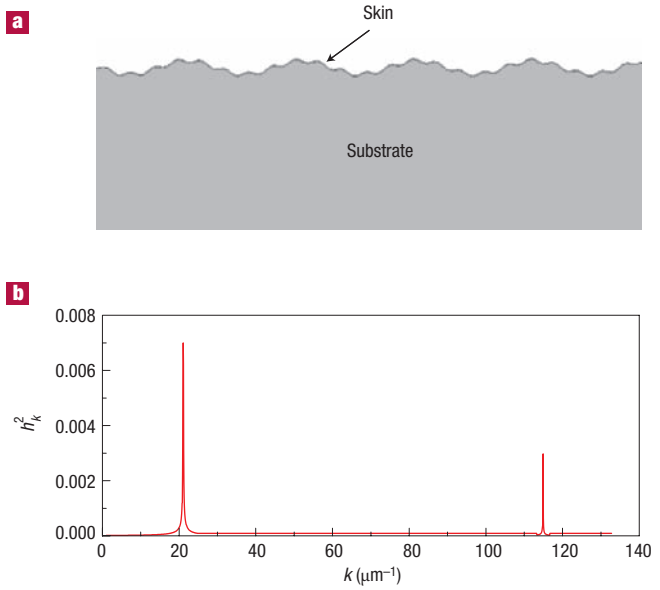


**Figure 3 Results of a finite element simulation of the skin + substrate system.** The skin is modelled as a Hookean linear elastic solid, whereas the substrate is modelled as an incompressible hyperelastic solid with a neo-Hookean constitutive relation (see Methods for details). When the substrate is subject to a uniform compressive strain, a periodic pattern of primary wrinkles of small wavelength appears on the skin. **a**, Under further loading, the amplitude of the first generation of wrinkles saturates and a secondary wrinkling pattern on much larger wavelength appears thus forming the hierarchical nested buckling pattern. **b**, A power spectrum of the free-surface height $h(x)$, showing the squared Fourier-amplitude $h_k^2$ as a function of the wavenumber $k = 2\pi/\lambda$ confirms the presence of two wavelengths. The wavelength of the first generations is 55 nm, in agreement with experiment, whereas that of the second generation is 320 nm, which is a factor of three less than the experimental value. The primary reason for this discrepancy is the lack of an accurate model of the nonlinear constitutive law for the substrate.

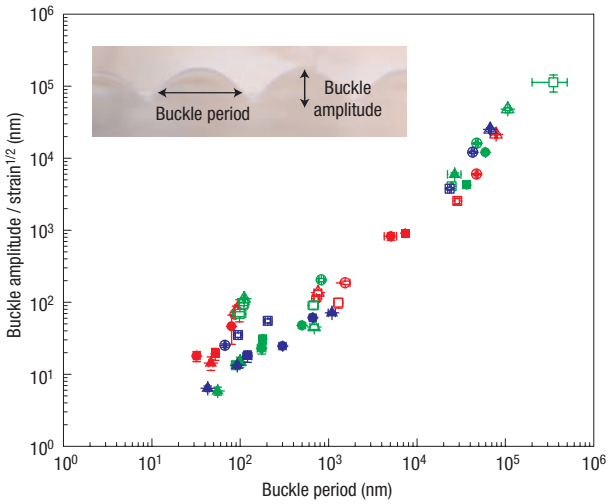


**Figure 4 Scaled buckle amplitude ($\zeta/\Delta^{1/2}$) plotted as a function of the buckle period ($\lambda$) on a log–log plot.** The symbols are the same as in Fig. 1. We see that the data collapse onto a straight line consistent with equation (2). The error bars are one standard deviation of the data.

thermal expansion between the skin and substrate[6,7], differential swelling or shrinkage[8], or differential growth of tissue (for example, human skin). Indeed, even if the skin/substrate system is subject to a simple compressive load, the skin will wrinkle in the same way due to the competition between the effects of bending the skin, which penalizes short wavelength buckles, and stretching the unmodified substrate (foundation), which penalizes long wavelengths[14,15]. This sets the stage for the amplitude of the primary wrinkles to grow as the applied strain is further relieved. Eventually the amplitude saturates owing to nonlinear effects in stretching and shearing the substrate. The composite of the wrinkled skin and the stretched substrate leads to the formation of an 'effective skin' that is now thicker and much stiffer than the original skin. Further release of the applied strain leads to additional effective compression; as a result, the composite skin buckles on a much larger length scale, creating a hierarchical buckled pattern. The formation of higher generation buckles continues until the strain is removed from the substrate. In an infinite system there is clearly no limit to this hierarchical patterning. Even in our finite system up to five generations of these hierarchical buckles are arranged in a nested manner; each buckle generation is a scaled-up version of the primary buckle (see Fig. 2). The smallest buckles are a few nanometres in wavelength, whereas the largest ones are almost a millimetre in size, thus spanning nearly five orders of magnitude in dimension.

To quantify this pattern, we summarize a classical calculation[14–16] here. The energy density per unit area for the rigid skin of thickness $h$ and modulus $E_S$, associated with bending it into a periodic array of wrinkles of wavelength $\lambda$ and amplitude $\zeta$ scales as $U_{bend} \approx E_S h^3 \zeta^2/\lambda^4$, whereas the stretching energy density of the substrate, having a modulus $E_B$, scales as $U_{stretch} \approx E_B \zeta^2/\lambda$ because the deformations decay exponentially into the bulk with a characteristic scale set by the wavelength[14,15]. The buckle amplitude is not independent of the wavelength owing to the ease of bending compared with stretching; this allows for deformations to be approximately inextensional, so that[16]:

$$(1+\frac{\zeta^2}{\lambda^2})^{1/2} - 1 \sim \Delta \quad , \tag{1}$$

where $\Delta$ is the applied external compressive strain. This last constraint implies that the amplitude of a wrinkle scales as[16]:

$$\zeta \sim \lambda \Delta^{1/2} \, . \tag{2}$$

Substituting the expression in (2) into the total energy per unit length $U_{total} \approx (U_{bend} + U_{stretch})\lambda$ and minimizing $U_{total}$ yields the well-known scaling law for the wavelength[14–16]:

$$\lambda \sim h\left(\frac{E_s}{E_B}\right)^{1/3} \, . \tag{3}$$

The ratio of Young's moduli $E_S/E_B$ was measured experimentally for our UVO-treated unstretched PDMS films (see Methods section for details). PDMS specimens treated with UVO for 30 and 60 minutes had $E_S/E_B$ equal to ~15 and ~87, respectively, which using equation (3) gives $\lambda \approx 12$ and 22 nm, respectively, for the two treatment times. From the data in Fig. 2, the estimated $\lambda$ corresponds roughly to the experimentally measured periods of the first generation of buckles (G1). To understand the formation of the next generation of buckles, we need to quantify the nonlinear saturation of the amplitude, which forms a thicker effective skin that then forms secondary wrinkles. This is accomplished by a finite element simulation of the system using a commercial package

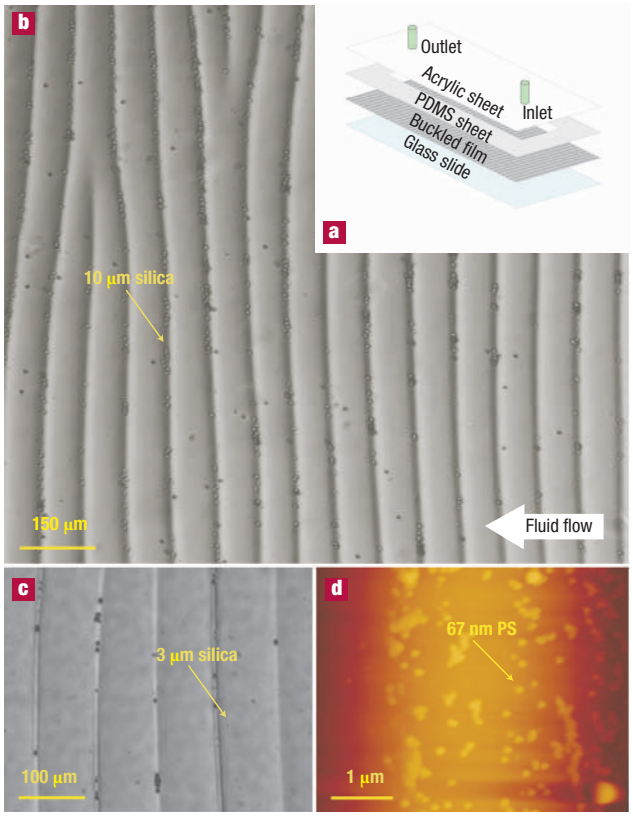


**Figure 5 Utilization of buckled substrates as microfluidic sieves.** **a**, Schematic of the structure of the microfluidic sieve with buckled film being the separating medium. **b–c**, Optical microscopy and **d**, SFM images of particle ordering on buckled surfaces. The buckled sheets were prepared by stretching PDMS films by $\Delta = 50\%$, exposing them to UVO for 30 minutes and instantaneously releasing the strain. A mixture of particles with three different sizes (≈10-μm and ≈3-μm silica and 67-nm polystyrene (PS) latex) in water was flown over the buckled surfaces in a microfluidic cell. The biggest silica particles ordered predominantly in the grooves between the G4 buckles (**b**). The intermediate sized particles were trapped in buckles with smaller periodicity that resided on top of the G4 buckles (**b** and **c**). The PS latex spheres formed 'particle chains' aligned along the buckle direction, presumably in the G2 or G3 buckles (**d**). The arrows indicate the positions of the individual particles within the buckled structure.

ABAQUS. The thin film is modelled as a linear elastic material, whereas the soft substrate is modelled as an incompressible hyperelastic material with a neo-Hookean constitutive law that accounts for the nonlinearity in the stress–strain relation in a simple way. The specific form of the constitutive relation is unimportant as long as there is an amplitude saturation effect that eventually makes it more expensive for the folds to grow than to wrinkle at a larger length scale to form a nested wrinkled pattern (for details, see Methods). To mimic the experiment, the substrate is subject to a uniform compressive strain leading to a strain mismatch between the skin and the substrate. In Fig. 3a, we show that as the applied strain on the substrate is increased beyond a critical value, secondary wrinkles appear. In Fig. 3b, we show the power spectrum of the height and confirm that there are two wavelengths in the system. This scenario repeats itself as the applied strain is increased even further, and confirms that the mechanism proposed above captures the essence of the phenomenon. In Fig. 4 we plot the scaled experimental buckle amplitude $\zeta/\Delta^{1/2}$ as a function of the buckle wavelength $\lambda$; all data collapse roughly on a master curve consistent with equation (2), allowing us to explain the amplitude-wavelength correlation as well.

Our results may also be relevant to observations in other systems. Mammalian skin consists of a thin stiff epidermis coating a thicker, softer dermis. When compressed, skin buckles into wrinkles on many different scales, consistent with our picture. Indeed, even the dermal ridges in our fingerprints are thought to arise from the relative growth between the two layers in the fetus[17] and thus may be explained in terms of the above ideas[18]. On a completely different length scale, in geology, these hierarchical folding patterns[19,20] are also well known but remain poorly understood; although our experiments and theoretical model are strictly relevant only for the simplest reversible elastic deformations, their essentially geometrical underpinnings suggest a mechanism for how irreversible hierarchical folds might arise in geology.

In addition to providing insight into mechanical behaviour of skins and wrinkling phenomena, the nested hierarchy of structural features can be effectively used in a wide range of potential devices. For instance, when covered with a thin layer of refractive material, such as metal, the buckled sheets can be used as tunable optical gratings[21]. The tunability of surface topography can be further supplemented with chemical grafting, which would involve deposition of organosilane-based self-assembled monolayers[22,23] or surface-grafting of polymers[24,25] on the silica surface. In this respect, the buckled surfaces can be tailored to act as biocompatible topographic matrices for cell alignment[26]. Nerve cells aligned by the buckled surfaces can facilitate directional signal transport over large distances[27]. In addition, the tunable corrugations offer the prospect of generating surfaces with adjustable roughness that can be used to control actively the frictional and adhesive properties.

We close with an account of one possible application that directly uses the hierarchical nature of the buckled structures: the separation of an aggregate of polydisperse particles into aligned linear chains of monodisperse particles. A buckled PDMS sheet was embedded inside a custom-designed microfluidic chamber shown schematically in Fig. 5a (for details see the Methods section) and a triphasic aqueous suspension comprising 10-μm and 3-μm silica beads and 67-nm polystyrene latex particles was pumped past the surface (perpendicular to the buckles) at a constant flow rate (varying from 0.1 to 1 $cm^3\ min^{-1}$). On entering the microfluidic separator, the particles began to segregate. Optical microscopy images confirmed that the 10-μm silica particle resided predominantly in the valleys of the G4 buckles (Fig. 5b) while a large fraction of the 3 μm silica particles resided on top of the smaller buckles, between two neighbouring G3 buckles (Fig. 5c). Finally, the smallest particles seem to align themselves in the valleys of the G2 buckles. This oriented segregation mechanism is suggestive of a means of forming linear chains that can be functional if the particles can be bonded using an external stimulus (UV radiation, heat, and so on).

Our account of these wrinkling patterns has, quite literally, only scratched the surface. Much remains to be done, and there are already hints that this method of controlled, reversible nested micropatterning opens up many venues for technological exploitation such as controlled wetting, adhesion and friction, all of which are crucially dependent on microscopic length scales and the topography of the underlying substrate.

## METHODS

Model PDMS networks used in this study were made by crosslinking nearly monodisperse PDMS vinyl-terminated chains ($M_n$ = 49.5 KDa, Gelest) with tetrakis dimethyl siloxy silane crosslinker in a ratio 1:1.7, which leads to 'ideal' PDMS networks with the highest elastic modulus[28]. The PDMS film was prepared and extracted using the same method as described in ref. 13.

The PDMS films were stretched uniaxially by $\Delta$ (equal to 30%, 50% and 70%) in a custom-built stretching apparatus[11]. The UVO treatment of the PDMS network surfaces was carried out in a

commercial UVO chamber (Jelight Company, model 42) using the process described in ref. 13. The stretcher with the PDMS specimens was placed into the UVO-cleaner tray at the distance of ~10 mm from the lamp and exposed to the radiation from one side only for different times (30, 60, and 90 minutes). The pressure, temperature, and relative humidity in the chamber were maintained at 1 atm, 20 °C, and 50–60%, respectively.

Scanning elecron microscopy images were recorded with a JEOL JSM-6400F microscope using secondary electron imaging on specimens previously covered with a ~5-nm-thick layer of platinum. Light microscopy images were collected using light microscope (Olympus BX-60) in the transmission mode on samples both during and after the strain release. After the strain release, the UVO-treated side of the PDMS samples was imprinted into an epoxy. After curing, the topography of the epoxy mould was imaged using SFM (Multimode Nanoscope III, Digital Instruments) in the contact mode and the tapping mode and also by profilometry (Alpha Step Surface Profiler 500, Tencor Instruments). The buckle profiles were mapped with lowest scanning speed and maximum resolution allowed by the profilometer in order to minimize the distortion of the sample surface. The analysis of the profile was completed for six different areas on the sample surface by averaging data for at least five most representative buckles. The periodicity of the buckles was determined from the SFM images both directly from each image and from the fast-Fourier-transform map of the SFM corresponding image. The periodicity and height of the buckles reported represent an average over ~15 buckles collected on different areas on each sample.

The elastic modulus of bare PDMS and PDMS-UVO was measured by indentation experiments using a SFM force-distance approach[29–31] and by using only the first 5 nm of compression, so as to measure only the surface modulus. All measurements were performed with the same cantilever, thus obtaining accurate relative moduli ($E_S/E_B$), using the neat elastomer as a reference; subsequent calibration of the cantilever's normal spring constant provided also absolute values for moduli[29]. Both a sharp atomic force microscope tip and a 10-μm tungsten sphere were used in these tests, giving the same results for the moduli values used herein.

The particle separation experiments were carried out in a custom-designed microfluidic channel formed by sandwiching the buckled PDMS sheet between a flat glass support and a 100-μm-thick PDMS spacer with a rectangular window; the latter was covered with a flat transparent acrylic cover. Inlet and outlet tubing attached to the acrylic sheet facilitated transport of a fluid, which was then flown across the buckled surface; the fluid flow inside the device was guided by the rectangular window in the PDMS spacer. Real-time particle motion across the buckled substrate was monitored with optical microscopy in the Nomarski mode.

The computations were carried out using ABAQUS, a commercial finite-element package, with the following parameter values: The substrate shear modulus $\mu = 0.34$ MPa, film thickness $h = 5$ nm, film Young's modulus $E_B = 120$ MPa. The wavelength of the first generations is 55 nm, in agreement with experiment, and that of the second generation 320 nm, which is a factor of three less than the experimental value. The primary reason for this discrepancy is the lack of an accurate model for the nonlinear constitutive law for the substrate. For simplicity, we have used a neo-Hookean model for the substrate with a free energy given by the strain energy function

$$W = \frac{\mu}{2}\sum_{i=1}^{3}(\lambda_i^2 - 3), \qquad (4)$$

where $\lambda_i$ are the principal stretches, which satisfy the relation $\lambda_1\lambda_2\lambda_3 = 1$ in light of incompressibility, and $\mu$ is the shear modulus of the material.

Received 7 December 2004; accepted 27 January 2005; published 6 March 2005.

## References


1. Hamers, R. J. Flexible electronic futures. *Nature* **412,** 489–490 (2001).
2. Lim, J. H., Lee, K. S., Kim, J. C. & Lee, B. H. Tunable fiber gratings fabricated in photonic crystal fiber by use of mechanical pressure. *Opt. Lett.* **29,** 331–333 (2004).
3. Wong, C. W. *et al.* Strain-tunable silicon photonic band gap microcavities in optical waveguides. *Appl. Phys. Lett.* **84,** 1242–1244 (2004).
4. Harris, A. K., Wild, P. & Stopak, D. Silicone rubber substrata: a new wrinkle in the study of cell locomotion. *Science* **208,** 177 (1980).
5. Stafford, C. M. *et al.* A buckling-based metrology for measuring the elastic moduli of polymeric thin films. *Nature Mater.* **3,** 545–550 (2004).
6. Bowden, N., Brittain, S., Evans, A. G., Hutchinson, J. W. & Whitesides, G. W. Spontaneous formation of ordered structures in thin films of metals supported on an elastomeric polymer. *Nature* **393,** 146–149 (1998).
7. Bowden, N., Huck, W. T.S, Paul, K. & Whitesides, G. W. The controlled formation of ordered, sinusoidal structures by plasma oxidation of an elastomeric polymer. *Appl. Phys. Lett.* **75,** 2557–2559 (1999).
8. Huck, W. T. S., Bowden, N., Onck, P., Pardoen, T., Hutchinson, J. W. & Whitesides, G. W. Ordering of spontaneously formed buckles on planar surfaces. *Langmuir* **16,** 3497–3501 (2000).
9. Cerda, E. & Mahadevan, L. Geometry and physics of wrinkling. *Phys. Rev. Lett.* **90,** 074302 (2003).
10. Hedden, R. C., Saxena, H. & Cohen, C. Mechanical properties and swelling behavior of end-linked poly(diethylsiloxane) networks. *Macromolecules* **33,** 8676–8684 (2000).
11. Genzer, J., Fischer, D. A. & Efimenko, K. Fabricating two-dimensional molecular gradients via asymmetric deformation of uniformly-coated elastomer sheets. *Adv. Mater.* **15,** 1545–1547 (2003).
12. Ouyang, M., Yuan, C., Muisener, R. J., Boulares, A. & Koberstein, J. T. Conversion of some siloxane polymers to silicon oxide by UV/ozone photochemical processes. *Chem. Mater.* **12,** 1591–1596 (2000).
13. Efimenko, K., Wallace, W. E. & Genzer, J. Surface modification of Sylgard-184 poly(dimethyl siloxane) networks by ultraviolet and ultraviolet/ozone treatment. *J. Colloid Interface Sci.* **254,** 306–315 (2002).
14. Allen, H. G. *Analysis and Design of Structural Sandwich Panels* (Pergamon, New York, 1969).
15. Landau, L. D. & Lifshitz, L. *Theory of Elasticity* 3rd edn (Pergamon, New York, 1986).
16. Cerda, E. & Mahadevan, L. Wrinkling of an elastic sheet under tension. *Nature* **419,** 579–580 (2003).
17. Babler, W. J. Embryologic development of epidermal ridges and their configurations. *Birth Defects Orig.* **27,** 95–112 (1991).
18. Kücken, M. & Newell, A. C. A model for fingerprint formation. *Europhys. Lett.* **68,** 141–146 (2004).
19. Price, N. J. & Cosgrove, J. W. *Analysis of Geological Structures* (Cambridge Univ. Press, Cambridge, 1990).
20. Huddleston, P. J. & Lan, L. Information from fold shapes. *J. Struct. Geology* **15,** 253–264 (1993).
21. Harrison, C., Stafford, C. M., Zhang, W. & Karim, A. Sinusoidal phase grating created by a tunably buckled surface. *Appl. Phys. Lett.* **85,** 4016–4018 (2004).
22. Ulman, A. Formation and structure of self-assembled monolayers. *Chem. Rev.* **96,** 1533–1554 (1996).
23. Schreiber, F. Structure and growth of self-assembling monolayers. *Prog. Surf. Sci.* **65,** 151–256 (2000).
24. Zhao, B. & Brittain, W. J. Polymer brushes: surface-immobilized macromolecules. *Prog. Polym. Sci.* **25,** 677–710 (2000).
25. Edmondson, S., Osborne, V. L. & Huck, W. T. S. Polymer brushes via surface-initiated polymerizations. *Chem. Soc. Rev.* **33,** 14–22 (2004).
26. Teixeira, A. I., Abrams, G. A., Bertics, P. J., Murphy, C. J. & Nealey, P. F. Epithelial contact guidance on well-defined micro- and nanostructured substrates. *J. Cell. Sci.* **116,** 1881–1892 (2003).
27. Hynes, R. O. & Lander, A. D. Contact and adhesive specificities in the associations, migrations, and targeting of cells and axons. *Cell* **68,** 303–322 (1992).
28. Patel, S. K., Malone, S., Cohen, C., Gilmor, K. R. & Colby, R. H. Elastic modulus and equilibrium swelling of poly(dimethylsiloxane) networks. *Macromolecules* **25,** 5241–5251 (1992).
29. Manias, E., Chen, J., Fang, N. & Zhang, X. Polymeric MEMS components with tunable stiffness. *Appl. Phys. Lett.* **79,** 1700–1702 (2001).
30. Radmacher, M., Fritz, M., Cleveland, J. P., Walters, D. A. & Hansma, P. K. Imaging adhesion forces and elasticity of lysozyme adsorbed on mica with the atomic force microscope. *Langmuir* **10,** 3809–3814 (1994).
31. Rotsch, C & Radmacher, M. Mapping local electrostatic forces with the atomic force microscope. *Langmuir* **13,** 2825–2832 (1997).


## Acknowledgements

The work was supported by the grants from the Camille & Henry Dreyfus Foundation (J.G.), the NER Program at the National Science Foundation (J.G., E.M.), and the Office of Naval Research (J.G., L.M.). We thank O.D. Velev for fruitful discussions.

Correspondence and requests for materials should be addressed to L.M. and J.G.

Supplementary Information accompanies the paper on www.nature.com/naturematerials.

## Competing financial interests

The authors declare that they have no competing financial interests.